

CIFIE 2010

# ON THE EFFECT OF INTERGRANULAR NANOCRACKS ON THE SHEAR-COUPLED MIGRATION OF TILT BOUNDARIES

A. IRASTORZA, A. LUQUE\*, J. ALDAZABAL, J.M. MARTÍNEZ-ESNAOLA, J. GIL SEVILLANO

CEIT and TECNUN (University of Navarra)  
Paseo Manuel de Lardizábal 15, 20018 San Sebastián. Spain  
\*aluque@ceit.es

**ABSTRACT:** In this work, we present molecular dynamics simulations of the shear-coupled migration behaviour of symmetrical tilt boundaries  $\Sigma 17(530)/[001]$  perturbed by the presence of nanocracks lying on the grain boundary. The simulations were performed for copper bicrystals at 300 K. The focus has been on the study of crack size effects. The simulations were carried out using the embedded atom method with temperature control. Systems of constant width,  $X$ , and different crack sizes,  $2a$ , were generated at 0 K. The ratio  $2a/X$  characterizes the system. Periodic boundary conditions were set along the direction of application of the load and the tilt axis. After relaxation, the virtual shear of the bicrystals was carried out at a constant rate of  $10^8 \text{ s}^{-1}$ . The response of the cracked specimens can be divided into: (i) shear-coupled migration of the grain boundary with increasing applied shear stress, (ii) intergranular propagation of the crack and (iii) emission of dislocations and closing of the grain boundary dislocation loop.

**Keywords:** Copper, molecular dynamics, shear-coupled migration, nanocracks, mode II loading.

**RESUMO:** Neste trabalho, apresentamos simulações de dinâmica molecular do comportamento de migração de uma fronteira de grão acoplada à aplicação de uma tensão de cisalhamento no caso de uma fronteira simétrica de flexão  $\Sigma 17(530)/[001]$  perturbada pela presença de nanofendas na própria fronteira de grão. As simulações foram realizadas para bicristais de cobre a 300 K. O interesse do estudo é o efeito do tamanho da fenda. As simulações foram realizadas utilizando o *embedded atom method* com controlo de temperatura. Sistemas de largura constante,  $X$ , e tamanhos de fendas diferentes,  $2a$ , foram gerados a 0 K. A razão  $2a/X$  caracteriza o sistema. Condições de fronteira periódicas foram estabelecidas ao longo da direção de aplicação da carga e do eixo da fronteira simétrica de flexão. Após o relaxamento, o cisalhamento virtual dos bicristais foi realizado a uma taxa constante de  $10^8 \text{ s}^{-1}$ . A resposta das amostras fissuradas pode ser dividida em: (i) ao cisalhamento acoplado a migração do limite de grão com o aumento da tensão de cisalhamento aplicada, (ii) propagação intergranular da fenda e (iii) emissão de deslocamentos e formação de deslocamentos em anel.

**Palavras chave:** Cobre, dinâmica molecular, migração acoplada ao cisalhamento, nanofendas, fratura modo II.

## 1. INTRODUCTION

Shear-coupled migration (SCM) [1–24] has been recognized as a particular plastic strain mechanism that can, in a wide range of temperatures, complement or compete with other plastic intra- or inter-granular mechanisms available to bicrystals or polycrystals, such as dislocation-mediated slip, grain boundary (GB) sliding, twinning... Conservative SCM of pure tilt boundaries is diffusionless. It occurs by collective atomic motion without recourse to long-range diffusion. The process is thermally activated but can take place at low temperatures. In fact, at these temperatures, it can be the dominant shear-driven GB migration mechanism.

This is maintained up to very high temperatures relative to the melting point, at least for high shear strain rates [16,19] before viscous-like creep processes become prevailing.

The SCM phenomenon implies that a consequence of an applied shear stress,  $\tau$ , the bicrystal shows two types of motions which are depicted in Fig. 1 [16,24]. The first one is a shear displacement, a movement of the upper crystal relative to the lower one parallel to the plane containing the boundary and characterized by the velocity  $v_{\parallel}$ . The second one is the migration of the GB, a movement perpendicular to the plane that contains the boundary and characterized by the migration velocity,  $v_{\perp}$ .

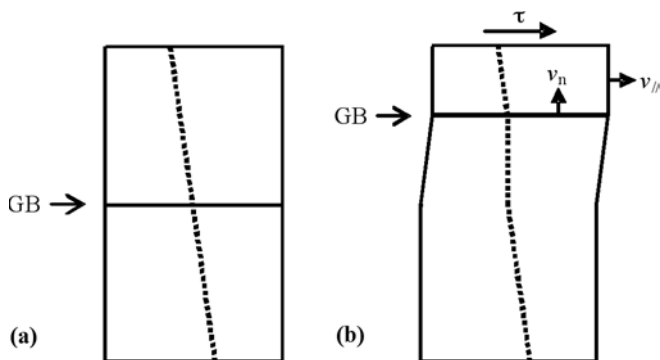


**Fig. 1.** SCM phenomenon in a planar boundary of a free bicrystal: (a) initial configuration and (b) after the application of a shear stress. The dotted lines permit following the response of the bicrystal [16]

The effectiveness of the applied shear stress in the SCM phenomenon can be characterized in terms of the shear coupling factor,  $\beta$ , defined as the ratio of the shear displacement parallel to the GB surface in the direction normal to the tilt axis to the GB migration normal to its surface, this is,

$$\beta = \frac{v_{\parallel}}{v_{\perp}} \quad (1)$$

Note that this definition of  $\beta$  corresponds also to the shear strain associated with the passage of the migrating boundary,  $\Gamma_{\text{SCM}}$  [23]. In this sense, a macroscopic plastic strain associated to SCM,  $d\bar{\epsilon}$ , is given by

$$d\bar{\epsilon} = \beta M_{\text{SCM}} dV_{\text{V}}^{\text{SCM}} \quad (2)$$

Where  $M_{\text{SCM}}$  is an orientation factor and  $V_{\text{V}}^{\text{SCM}}$  is the volume fraction swept by the migrating boundary. Like GB sliding or pure diffusional deformation, SCM is not a self-sufficient plastic mechanism for arbitrary deformation of polycrystals. Hence, it always needs to be complemented by the activity of other deformations mechanisms to provide compatible large deformations of grain aggregates [23].

Some authors [16] have proposed a geometrical model based on the dislocation content of the symmetrical tilt boundary which permits obtaining  $\beta$  in terms of the GB misorientation,  $\theta$ , as

$$\beta = 2 \tan\left(\frac{\phi}{2}\right) \quad (3.a)$$

$$\beta = -2 \tan\left(\frac{\pi}{4} - \frac{\phi}{2}\right) \quad (3.b)$$

Eq. 3.a applies to “low” misorientations and produces a “positive” coupling between the applied shear stress and the GB migration, this is, GB moves upwards when  $\tau$  is applied to the right. Eq. 3.b applies to “high” misorientations and produces a “negative” coupling, this is, the GB migration occurs in the opposite sense compared to “positive” coupling. The transition between these two behaviours takes place at  $\phi \approx 35^{\circ}$ - $40^{\circ}$  [16,17]. The shear coupling factor is related to the tilt misorientation through the Frank–Bilby vector, which captures the net dislocation content of the GB:  $\langle 100 \rangle$  dislocations for low misorientations and  $\langle 110 \rangle$  dislocations for high misorientations, as derived from the Frank–Bilby equation [26]. How-

ever, this equation yields a multiplicity of geometrically possible coupling factors and, from the structural point of view, a multiplicity of geometrically possible GB dislocation sets. For coincident or near-coincident boundaries, these sets are perfect dislocations of the crystal lattice and the displacement shift complete lattice.

First references to GB movement as a consequence of applied mechanical loads can be found in 1950s [1-3] and 1970s [4-7] for small- and high-angle tilt boundaries, respectively. The current burst of interest, both experimental [8-13] and numerical-theoretical [14-25], on SCM is due to its active role in the mechanical behaviour of nanograined materials and in the structural changes taking place in such materials when subjected to stress at low temperatures. SCM requires high resolved shear stresses that cannot be reached in polycrystals with conventional grain size before attaining the activation stress for profuse dislocation glide. In this kind of materials, observance of the Hall-Petch relationship is the key point for the dominance of low-temperature intragranular plastic mechanisms over intergranular plastic processes. However, in nanomaterials, inversion of the Hall – Petch effect can be observed [23]. Some other examples of SCM activity are grain growth during nanoindentation and near loaded crack tips, and fatigue of nanograined materials, as reviewed in Ref. 23. Therefore, a good understanding and mastering of SCM in nanostructured materials is essential to warrant their structural stability.

In this work, we present molecular dynamics (MD) simulations of the SCM behaviour of the symmetrical tilt boundary  $\Sigma 17(530)$  perturbed by the presence of nanocracks lying on the GB. The simulations have been performed for copper bicrystals at 300 K. We have compared the behaviour of a perfect boundary with the behaviour of a GB presenting nanocracks. We have also studied the crack size effect on this kind of systems.

## 2. SIMULATION CHARACTERISTICS

### 2.1. Molecular dynamics technique

The MD technique used for these atomistic simulations was the embedded atom method (EAM), proposed by Daw and Baskes [27,28]. The potentials that we have used in this EAM approach correspond to copper, obtained from Mishin *et al.* [29]. In essence, the EAM considers that each atom of the system is embedded in the network formed by the rest of atoms of the system and that they interact with their surrounding in terms of a nuclear interaction (the pair potential) and an electron-nucleus interaction (the so-called embedding potential). Further details of both this MD technique and these potentials can be found elsewhere [30,31]. It is particularly important to mention the existence of a cut-off radius,  $r_{\text{cut}}$ , for these atomic interactions. This parameter equals 0.55 nm for the copper potentials proposed by Mishin *et al.*

On one hand, for the numerical integration of the motion equations, we use a modified Verlet algorithm [32], as this

numerical integrator is simple, computationally inexpensive and sufficiently accurate. The time increment,  $\Delta t$ , employed for numerically obtain the atomic trajectories equals  $2.5 \times 10^{-15}$  s. Note that this is one of the most important drawbacks of atomistic simulations: time increments have to be necessarily small, to avoid numerical artifacts and divergences, and this limits the effective time span of the simulations.

On the other hand, the Nosé-Hoover thermostat [33,34] was implemented to control the system temperature,  $T$ . Essentially, the thermostat maintains the atomic velocities within an adequate range of values, according to the thermal energy of the system. This is obtained thanks to the convenient modification of the accelerations of the atoms, after each simulation step. In the case of these simulations,  $T$  equals 300 K.

## 2.2. The $\Sigma 17(530)/[001]$ tilt boundary

In this work, the generated bicrystals present a symmetrical tilt boundary  $\Sigma 17(530)/[001]$ .  $\Sigma$  is the relationship between the number of lattice points in a unit cell of the generating lattice and the number of lattice points in a unit cell of the coincidence site lattice (CSL). The first Miller indices after  $\Sigma 17$ , namely (530), indicate the plane where the GB lies. Its normal corresponds to the  $y$  axis of the simulation system. The following Miller indices, namely  $[001]$ , are the tilt axis and correspond to the  $-z$  direction of the simulation system. In the simulations that a crack had to be introduced, this is contained in the plane (530) and the crack tip lies along the  $[001]$  direction. The symmetrical tilt boundary  $\Sigma 17(530)$  corresponds to a high-angle misorientation of  $\varphi = 61.9^\circ$ . According to Eq. 3.b, this misorientation yields a shear coupling factor of  $\beta = -0.5$  for the case of a planar free GB. Note that the obtained shear coupling factor is negative, thus, we will observe the GB moving downwards when the shear stress is applied to the right.

## 2.3. Specimen generation and test features

Two types of bicrystals were generated for this work, namely, uncracked and cracked bicrystals. In all of the cases, the samples were constructed at 0 K. For both types of samples, the number of specimens is three. For the uncracked samples, the system dimensions changed from one specimen to another. In particular, the  $X$  dimension is 4.2 nm, 10.6 nm or 14.9 nm; respectively, the  $Y$  dimension is 8.4 nm, 21.1 nm or 29.2 nm; and, in all cases, the  $Z$  dimension is 2.2 nm. In the case of the cracked specimens, sample dimensions are the same, namely,  $10.6 \text{ nm} \times 2.2 \text{ nm} \times 21.1 \text{ nm}$ . Nanocracks were formed by removing the atoms located in a band of 0.55 nm of thickness, centred in the GB, along  $1/2$ ,  $1/3$  and  $1/4$  of the specimen size along the  $x$  axis. Thus,  $2a/X$  equals  $1/2$ ,  $1/3$  and  $1/4$  (see Fig. 2). The change of the  $2a/X$  ratio will permit us studying the effect of the crack size on the mechanical behaviour of these cracked samples.

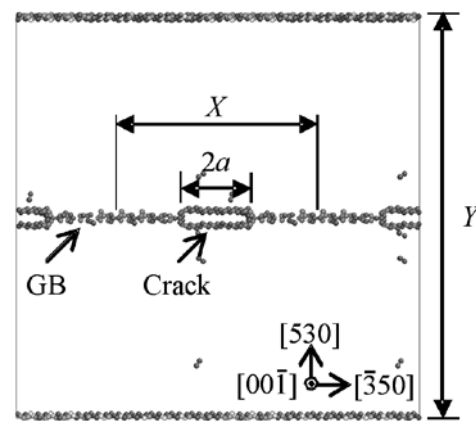


**Fig. 2.** Initial configuration of the cracked copper bicrystals presenting a symmetrical tilt boundary  $\Sigma 17(530)/[001]$ . The case of  $2a/X = 1/3$  is shown.

After generation of the bicrystals, the samples were relaxed to let the GB acquire a metastable configuration. The relaxation process proceeded at 0 K during 5 ps. Then, the temperature was increased linearly up to 300 K during 7.5 ps. Finally, the samples were kept at 300 K for 12.5 ps. Surface tension leads to some global and local geometrical distortion of the initial shape, particularly, around the crack tip, where tensional instabilities may appear.

After relaxation, two rigid zones of 0.55 nm of thickness were set in the upper and lower layers of the sample. During the simulations, carried out under displacement control, the lower layer remained fixed, whereas the upper rigid zone was displaced along the  $x$  axis at constant speed of  $v_{\parallel} \approx 2.1 \text{ m s}^{-1}$ . This corresponds to a shear strain rate,  $\dot{\gamma}$ , of  $10^8 \text{ s}^{-1}$ . The rest of the atoms of the system can move freely. Periodic boundary conditions (PBC) were set along the  $x$  and  $z$  axes. Thus, the specimens are in fact periodically cracked samples, as shown in Fig. 2.

A comment should be made about  $\dot{\gamma}$ . The high values of this parameter are inherent to MD simulations. Note that, although the applied displacements may be small (of the order of picometres), because of the nanometric systems considered and the small time steps assigned (of the order of femtoseconds), the effective strain rates will range between  $10^8 \text{ s}^{-1}$  and  $10^{10} \text{ s}^{-1}$ . Only the use of especial, more demanding algorithms, such as the so-called accelerated MD [18], permits reaching lower strain rate values.

The imposed shear displacement and the resulting required force were stored during the simulations, in order to compute the shear stress *vs.* shear strain  $\tau$ - $\gamma$  curves. Atomic positions were also periodically stored to analyse any structural changes that may occur, such as GB migration and slip, dislocation nucleation and emission or crack propagation. The visualization of the atomic systems is done making use of the atomic configuration viewer called AtomEye, provided by Li [35].

## 3. RESULTS AND DISCUSSION

### 3.1. The calculation of stresses

Before presenting the results of these simulations, we will briefly explain the method used for the calculation of the

applied stress. The so-called virial expression [36] permits computing the applied (global) stress tensor,  $\sigma_\infty$ , this is,

$$\sigma_\infty = \frac{1}{V} \sum_{i=1}^N \left( m \mathbf{v}_i \otimes \mathbf{v}_i - \frac{1}{2} \sum_{j \neq i} \mathbf{r}_{ij} \otimes \mathbf{f}_{ij} \right) \quad (4)$$

where  $V$  is the system volume,  $m$  is the atomic mass,  $\mathbf{v}_i$  is the velocity of atom  $i$ ,  $\mathbf{r}_{ij}$  is the distance vector between atoms  $i$  and  $j$  and  $\mathbf{f}_{ij}$  is the force between these two atoms. The result of the tensor product  $\mathbf{a} \otimes \mathbf{b}$  is a matrix  $\mathbf{C}$  such that each matrix element  $C_{hk} = a_h \cdot b_k$  ( $h, k = x, y, z$ ). Thus, the applied shear stress  $\tau$  corresponds to the term  $\tau_{xy}$  of the global stress tensor  $\sigma_\infty$ .

The virial theorem is generally applied to each atom to get a local stress tensor. However, some authors have developed a more accurate way of representing local stresses [37,38], namely

$$\sigma = \frac{1}{\Omega} \left( \Lambda_i (m \mathbf{v}_i \otimes \mathbf{v}_i) - \frac{1}{2} \sum_{j \neq i} \lambda_{ij} (\mathbf{r}_{ij} \otimes \mathbf{f}_{ij}) \right) \quad (5)$$

where  $\Omega$  is the volume of some representative partition element,  $\Lambda_i$  equals 1 if atom  $i$  is within the volume element and 0 otherwise, and  $\lambda_{ij}$  is the fraction of the length of the bond between atoms  $i$  and  $j$  lying within the volume element. In this work, we have chosen the volume element to be a sphere of radius equal to the copper lattice parameter,  $a = 0.36$  nm, centred on each atom. Therefore, each  $\sigma$  can be associated to the local stress at the position of the central atom.

### 3.2. Uncracked samples

Fig. 3 shows the  $\tau$ - $\gamma$  responses for the three uncracked bicrystals simulated at 300 K. The discussion of the main results corresponding to the uncracked configuration of the symmetrical tilt boundary  $\Sigma 17(530)$  can be found elsewhere [23,24]. However, it is important to note that:

- A negative coupling is observed: the GB migrates downwards when the shear stress  $\tau$  is applied to the right. A shear coupling factor  $\beta$  approximately equal to  $-0.5$  is computed.
- The slopes of the intermittent elastic loading stages are very similar to the elastic shear modulus, namely  $G = 27.3$  GPa, for a single crystal [39] with the same orientation as the samples and considering the elastic anisotropy of copper [40].
- The SCM is associated to a stick-slip phenomenon characterized by the overcoming of a critical value of applied shear stress, namely  $\tau_c \approx 0.4$  GPa [18,23,24], although a size effect can be observed in that parameter, according to Fig. 3.

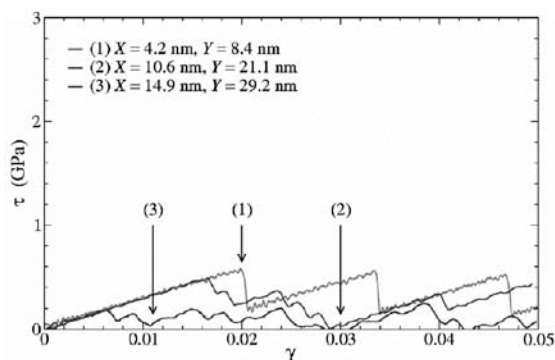


**Fig. 3.** Shear stress,  $\tau$ , vs. shear strain,  $\gamma$ , curves at 300 K of the uncracked copper bicrystals presenting a symmetrical tilt boundary  $\Sigma 17(530)/[001]$ .

### 3.3. Cracked samples

Fig. 4 shows the  $\tau$ - $\gamma$  responses for the three cracked bicrystals simulated at 300 K. Besides, Table 1 summarizes some relevant mechanical properties of these samples, namely the shear modulus,  $G$ , the shear stress and the shear strain for crack propagation,  $\tau_{\text{prop}}$  and  $\gamma_{\text{prop}}$ , respectively, the maximum applied shear stress,  $\tau_{\text{max}}$ , and the shear strain at the maximum shear stress,  $\gamma_{\text{max}}$ . The first thing that we can observe in Fig. 4 is that the presence of cracks significantly affects their mechanical response. Surprisingly, the cracked samples are strengthened by the intergranular cracks. In the following sections, we detail and explain this behaviour.

#### 3.3.1. SCM behaviour

Fig. 4 shows that the cracked samples behave as uncracked specimens do [23,24]. This is, they behave elastically, with the values of shear modulus  $G$  summarized in Table 1. When a critical value of applied shear stress  $\tau$  is overcome, the SCM of the GB occurs, showing the same stick-slip behaviour observed in the uncracked samples. This is the main deformation mechanism while  $\gamma$  is lower than 0.05 or 0.07, depending on the specimen considered. Unlike the uncracked samples, the applied shear stress does not remain at a low level. It needs to be increased for producing further deformation of the cracked sample. This is caused by the intergranular cracks which pin the GB [41,42]. Thus, the SCM can only take place away from the crack tips and that makes the GB to bow out, downwards, as shown in Fig. 5, because  $\beta$  is negative for the studied symmetrical tilt boundary. The misorientation between the GB and the crack tip progressively increases and, therefore, further GB migration becomes more and more complicated [24].

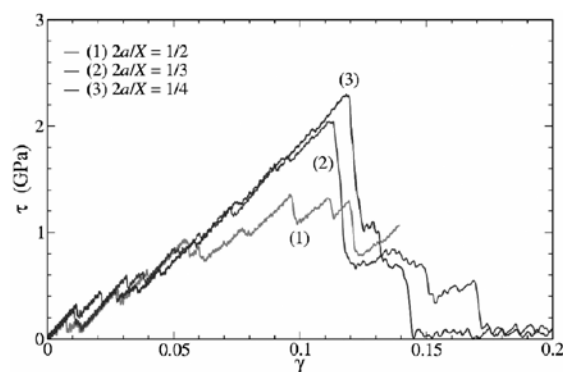


**Fig. 4.** Shear stress,  $\tau$ , vs. shear strain,  $\gamma$ , curves at 300 K of the cracked copper bicrystals presenting a symmetrical tilt boundary  $\Sigma 17(530)/[001]$ .

**Table 1.** Summary of the mechanical properties of the cracked copper bicrystals presenting a symmetrical tilt boundary  $\Sigma 17(530)/[001]$  at 300 K.

	(1) $2a/X = 1/2$	(2) $2a/X = 1/3$	(3) $2a/X = 1/4$
$G$ (GPa)	24.3	26.3	28.6
$\tau_{\text{prop}}$ (GPa)	0.93	1.24	–
$\gamma_{\text{prop}}$ @ $\tau_{\text{prop}}$	0.055	0.073	–
$\tau_{\text{max}}$ (GPa)	1.35	2.04	2.29
$\gamma_{\text{max}}$ @ $\tau_{\text{max}}$	0.096	0.111	0.119



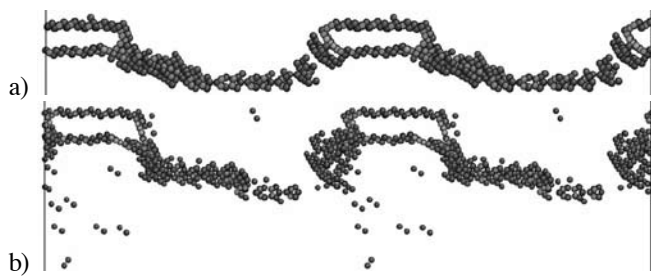


**Fig. 5.** Detail of the cracked copper bicrystal ( $2a/X = 1/3$ ) presenting a symmetrical tilt boundary  $\Sigma 17(530)/[001]$  at 300 K with (a)  $\gamma = 0.071$  (the GB bows out), and (b)  $\gamma = 0.11$  (the crack propagates, the GB keeps on migrating)

### 3.3.2. Crack propagation

When the angle formed by the GB and the crack plane is  $\sim 31^\circ$ , a different deformation mechanism activates. The propagation of the crack through the GB can be observed. That occurs at  $\gamma = 0.055$  and  $\gamma = 0.073$  for the samples with  $2a/X = 1/2$  and  $2a/X = 1/3$ , respectively. However, it does not take place in the sample with  $2a/X = 1/4$ . Therefore, there must also be

a significant contribution of the crack length (the  $2a/X$  ratio) and the stress concentration at the crack plane. As shown in Fig. 5.b, the crack opening near the crack tip produces different events of intergranular fracture along the GB when it lies on a (100) plane, indicating a possible ductile fracture. Further crack propagation is hindered and the SCM mechanism is enabled again.

We are going to analyse the stress distribution ahead of the crack front ( $\theta = 0$ ), too. For that, we first calculate the local stress associated to the atoms, according to Eq. 4. However, we have already mentioned that the crack advances at a particular angle. Therefore, we have to rotate the obtained stress tensor to a coordinate system as the one depicted in Fig. 6. This coordinate system is such that the crack propagation occurs along the 1 direction. Note that, in all of the cases, the components  $\tau_{13}$ ,  $\tau_{23}$  and  $\tau_{33}$  of the local stress tensor, are nearly zero or small compared with the other stress terms. Therefore, they are not presented here. The rest of stress terms are shown in Fig. 6.

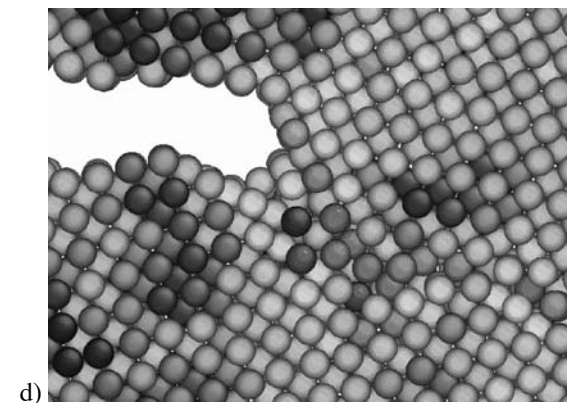
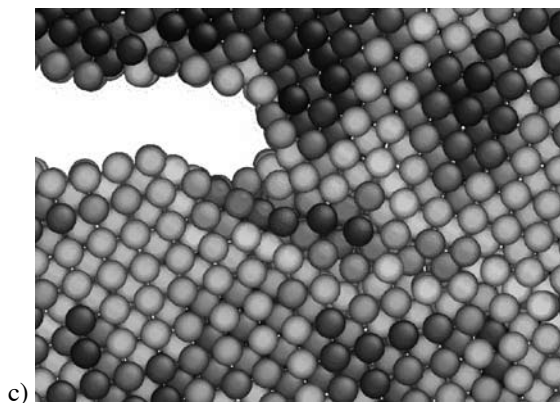
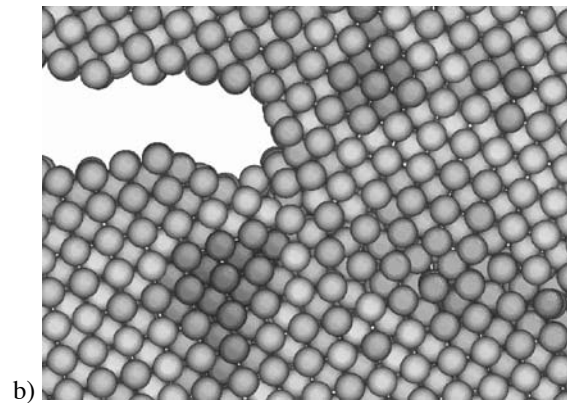
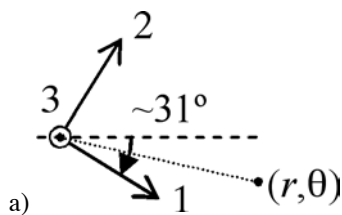


**Fig. 6.** (a) Local coordinate system for the crack study [29]. (b)  $\sigma_1$ , (c)  $\tau_{12}$  and (d)  $\sigma_2$ , for the cracked copper bicrystal ( $2a/X = 1/3$ ) presenting a symmetrical tilt boundary  $\Sigma 17(530)/[001]$  with  $\gamma = 0.074$  at 300 K.

Fig. 7 shows the stress distribution ahead of the crack for the samples which showed crack propagation. In Fig. 7, for each simulation, two different groups of data have been collected: the data series labelled “Up” refer to atoms just above the (100) plane (the crack propagation plane) and lying along the [010] direction, and the label “Down” refers to atoms just below the (001) plane and lying along [010]. Note that the curves depicted in Fig. 7 represent the values of  $\sigma_1$ ,  $\tau_{12}$  and  $\sigma_2$ ,

averaged along the  $z$  axis, at different distances from the crack tip,  $r$ . However, it should also be reminded that, naturally to the atomistic simulations, the position of the “crack tip” is not well defined, and that concepts such as “sharp crack” have no sense here. However, the position of crack tip can be bounded in the plane of the crack propagation. For this reason, the origin of the distances to the crack tip has been considered as a parameter in the fits shown in Fig. 7.

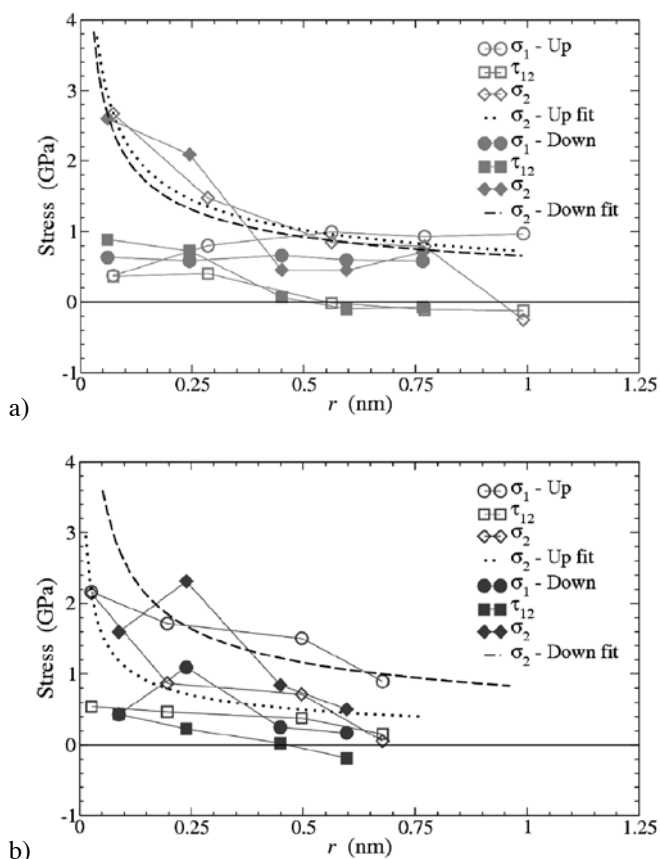


**Fig. 7.** Stress distribution as a function of the distance to the crack tip,  $r$ : (a)  $2a/X = 1/2$  and (b)  $2a/X = 1/3$ , at the corresponding  $\gamma_{prop}$  (see Table 1). The power-law fits of  $\sigma_2$ , namely  $\sigma_2 \propto r^{-\lambda}$ , are also shown.

These curves show that  $\sigma_2$  can be fitted with a power-law function of  $r$ . Note that the fit of the cracked bicrystal of  $2a/X = 1/2$  (Fig. 7.a) is particularly good and consistent above and below the propagation plane. For both samples,  $\sigma_2 \propto r^{-\lambda}$ , with the stress singularity exponent,  $\lambda = 1/2$ . This is in line with other atomistic fracture results which indicate that it is possible to express the opening displacement,  $\Delta u_2$ , of the atoms of the crack faces ( $\theta = \pm\pi$ ) near the crack tip ( $r < 3$  nm) in terms of  $r^{1/2}$  [30,31], this is,

$$\Delta u_2 = u_2(r, \theta = \pm\pi) - u_2(0, 0) = \pm K_{Ic} f \sqrt{r} \quad (5)$$

where  $u_2(0, 0)$  represents the degree of freedom related to the location of the crack tip and  $f$  is a coefficient which depends on the elastic properties of the material. The results of this work indicate that not only opening displacements but also the normal stress (with respect to the crack plane) can be fitted with the linear elastic solution proposed in the continuum for a sharp crack [43,44]. Therefore, we can validate the well-established continuum approach of fracture processes also on the basis of the results observed in this work attending to the atomic structure of materials.

The fits obtained considering Fig. 7 yield a critical stress intensity factor,  $K_{Ic}$ , ranging between 30 kPa $\sqrt{m}$  and 65 kPa $\sqrt{m}$ . Although small, these values are of the same order of other stress intensity factors calculated on a stress basis and reported in the literature for heterogeneous dislocation nucleation in a different crystal orientation but at the same temperature [30,31]. This may indicate that the observed crack propagation is a dislocation-mediated process, and, thus, ductile, in

which the generated dislocations are accommodated in the GB as they are emitted. In turn, dislocation generation would help explain why SCM is active after crack propagation.

### 3.3.3. Closing of the GB

As mentioned, the SCM mechanism is enabled again as consequence of the dislocation activity in the sample. When crack propagation stops and, as shown in Fig. 4, the applied shear stress is as high as 2 GPa (see Table 1), the emission of dislocations from the GB takes place (see Fig. 8.a) [24]. That occurs at  $\gamma = 0.111$  and  $\gamma = 0.119$  for the samples with  $2a/X = 1/3$  and  $2a/X = 1/4$ , respectively. However, it is not observed in the cracked sample of  $2a/X = 1/2$  as  $\tau$  is not high enough.

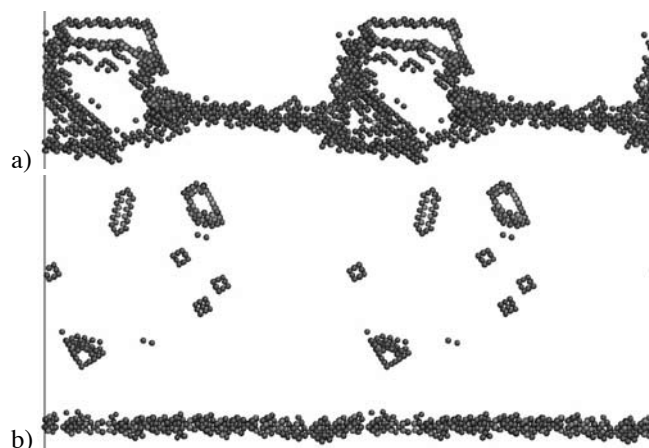


**Fig. 8.** Detail of the cracked copper bicrystal ( $2a/X = 1/3$ ) presenting a symmetrical tilt boundary  $\Sigma 17(530)/[001]$  at 300 K with (a)  $\gamma = 0.116$  (partial dislocation emission and closing of the GB), and (b)  $\gamma = 0.2$  (the GB is free from the crack and other obstacles).

The dislocations emitted during this step of the simulation are partial dislocations in the  $\{111\}\langle 211 \rangle$  system. As it can be seen in Fig. 8.a, they propagate in the lower crystal until they permit closing the GB dislocation loop. This implies the formation of a new GB below the crack and, thus, the pinning effect exerted by the crack starts to disappear. In the case of the cracked sample of  $2a/X = 1/3$ , this process is helped by the reduction of the crack size, as shown in Fig. 8.b. Nevertheless, the sample of  $2a/X = 1/4$  does not show that crack size reduction. Once the GB gets to detach from the crack (and from other softer obstacles formed during the unpinning process: note, in Fig. 4, the differences in the  $\tau$ - $\gamma$  response after the big stress drop in these two cracked samples), the boundary configuration of the cracked specimens and the GB of the uncracked bicrystals look very much alike. Therefore, further deformation of the samples produces SCM of the GB at shear stresses of the same order of the  $\tau_c$  observed in the uncracked samples.

Finally, it is worth mentioning that, in the cracked sample of  $2a/X = 1/2$ , as the nucleation of dislocations does not occur, the SCM of the GB cannot be enabled again. Nevertheless, a different mechanism activates in order to accommodate the introduced deformation. That mechanism is the GB slip [24], which is also possible due to the reduced dimension of the ligament. As a consequence, the crack shape changes, as shown in Fig. 9.



**Fig. 9.** Detail of the cracked copper bicrystal ( $2a/X = 1/2$ ) presenting a symmetrical tilt boundary  $\Sigma 17(530)/[001]$  at 300 K with (a)  $\gamma = 0.11$  (before GB slip), and (b)  $\gamma = 0.138$  (after GB slip).

#### 4. CONCLUSIONS

The shear-coupled migration of the symmetrical tilt boundary  $\Sigma 17(530)/[001]$  perturbed by nanocracks lying on the grain boundary has been studied by means of molecular dynamics simulations of copper bicrystals at 300 K.

The presence of intergranular nanocracks on the grain boundary produces the hindering of the shear-coupled migration behaviour of the analysed  $\Sigma 17(530)/[001]$  boundary. The tilt boundary is pinned by the crack tip and migration can only occur in association with the bowing-out of the grain boundary, downwards, as it corresponds to its negative shear-coupling factor,  $\beta$ . The applied stress needs to be increased above the critical shear stress value that makes a flat boundary migrate. Hence, nanocracks strengthen the material.

However, intergranular crack propagation is also observed. We have determined that crack propagation permits further advance of the grain boundary. We have reasonably fitted the stress ahead of the crack with  $r^{-1/2}$ , as proposed within the linear elastic solution for sharp cracks in continuum solids. Therefore, this result establishes a definite link between the atomistic world and the continuum approach.

The applied shear stress grows until new plastic-deformation mechanisms activate, in order to accommodate larger deformations. In particular, we have observed dislocation emission from the grain boundary or grain boundary sliding, depending on the ligament size of the sample. In the case that there is emission of dislocations, this takes place at the same time as shear-coupled migration. For this reason, the boundary can eventually detach from the crack tip.

#### ACKNOWLEDGMENTS

This work was supported by the Basque Government (Etorrek inanoGUNE IE08-225 and IE09-243) and the Spanish Ministry of Science and Innovation (Consolider nanoGUNE CSD2006 – 0053).

#### REFERENCES

[1] J. Washburn, E.R. Parker, *J. Metals AIME Trans.* 4 (1952) 1076.

[2] C.H. Li, E.H. Edwards, E.R. Parker, *Acta Metall.* 1 (1953) 223-229.

[3] D. McLean, *Nature* 172 (1953) 300-301.

[4] D.W. Bainbridge, C.H. Li, E.H. Edwards, *Acta Metall.* 2 (1954) 322-333.

[5] S.G. Khayutin, *Phys. Met. Metallogr.* 37 (1974) 161.

[6] M. Guillopé, J.P. Poirier, *Acta Metall.* 28 (1980) 163-167.

[7] W.D. Means, M.W. Jessell, *Tectonophysics* 127 (1986) 67-86.

[8] M.W. Jessell, *J. Struct. Geology* 8 (1986) 527-542.

[9] M. Wining, G. Gottstein, L.S. Shvindlerman, *Acta Mater.* 49 (2001) 211-219.

[10] M. Wining, G. Gottstein, L.S. Shvindlerman, *Acta Mater.* 50 (2002) 353-363.

[11] M. Wining, *Acta Mater.* 51 (2003) 6465-6475.

[12] S. Zaeferrer, J.C. Kuo, Z. Zhao, M. Wining, D. Raabe, *Acta Mater.* 51 (2003) 4719-4735

[13] S. Badirujjaman, X.W. Li, M. Wining, *Mater. Sci. Eng. A* 448 (2007) 242-248.

[14] J.W. Cahn, J.E. Taylor, *Acta Mater.* 52 (2004) 4887-4898.

[15] F. Sansoz, J.F. Molinari, *Acta Mater.* 53 (2005) 1931-1944.

[16] J.W. Cahn, Y. Mishin, Y. A. Suzuki, *Acta Mater.* 54 (2006) 4953-4975.

[17] J.W. Cahn, Y. Mishin, Y. A. Suzuki, *Philos. Mag.* 86 (2006) 3965-3980.

[18] Y. Mishin, A. Suzuki, B.P. Uberuaga, A.F. Voter, *Phys. Rev. B* 75 (2007) 224101/1-7.

[19] D.A. Molodov, V.A. Ivanov, G. Gottstein, G., *Acta Mater.* 55 (2007) 1843-1848.

[20] M. Wining, M., *Philos. Mag.* 87 (2007) 5017-5031.

[21] V.A. Ivanov, Y. Mishin, *Phys. Rev. B* 78 (2008) 064106/1-12.

[22] H. Zhang, D. Du, D. D.J. Srolovitz, *Philos. Mag.* 88 (2008) 243-256.

[23] A. Luque, J. Aldazabal, J.M. Martínez-Esnaola, J. Gil Sevillano, *Phys. Status Solidi C* 6 (2009) 2107-2112.

[24] A. Luque, J. Aldazabal, J.M. Martínez-Esnaola, J. Gil Sevillano, *Philos. Mag.* (2010). DOI: 10.1080/14786430903097715.

- [25] A. Irastorza, A. Luque, J. Aldazabal, J.M. Martínez-Esnaola, J. Gil Sevillano, *Anales de Mecánica de la Fractura* 27 (2010) 491-496.
- [26] A.P. Sutton, R.W. Baluffi, *Interfaces in Crystalline Materials* (1995) Clarendon Press.
- [27] M.S. Daw, M.I. Baskes, *Phys. Rev. Lett.*, 50 (1983) 1258-1288.
- [28] M.S. Daw, M.I. Baskes, *Phys. Rev. B*, 29 (1984) 6443-6453.
- [29] Y. Mishin, D. Farkas, M.J. Mehl, D.A. Papaconstatopoulos, *Phys. Rev. B*, 63 (2001) 224106/1-6.
- [30] A. Luque, J. Aldazabal, J.M. Martínez-Esnaola, J. Gil Sevillano, *Fatigue Fract. Engng. Mater. Struct.*, 29 (2006) 615-622.
- [31] A. Luque, J. Aldazabal, J.M. Martínez-Esnaola, J. Gil Sevillano, *Fatigue Fract. Engng. Mater. Struct.*, 30 (2007) 1008-1015.
- [32] D. Raabe, *Computational Materials Science* (1988) Wiley-VCH.
- [33] S. Nosé, *J. Chem. Phys.* 81 (1984) 511-519.
- [34] W.G. Hoover, *Phys. Rev. A*, 31 (1985) 1695-1697.
- [35] J. Li, *Modell. Simul. Mater. Sci. Eng.* 11 (2003) 173-177, 2003.
- [36] Z.H. Sun, X.X. Wang, A.K. Soh, A.K., H.A. Wu, *Modell. Simul. Mater. Sci. Eng.* 14 (2006) 423-431.
- [37] H. van Swygenhoven, P.M. Derlet, *Dislocations in Solids* (2008), 1-42, Eds. J. Hirth.
- [38] J. Cormier, J.M. Rickman, T.J. Delph, *J. Appl. Phys.* 89 (2001) 99-104.
- [39] A.A. Sharif, F. Chu, A. Misra, T.E. Mitchell, J.J. Petrovic, *J. Am. Ceram. Soc.* 83 (2000) 2246-2250.
- [40] W.F. Gale, W.F. Totemeier, *Smithells Metal Reference Book* (2004) Elsevier.
- [41] R.O. Scattergood, D.J. Bacon, *Acta Metall.* 30 (1982) 1665-1677.
- [42] Y.N. Osetsky, D.J. Bacon, *Mater. Sci. Eng. A* 400/401 (2005) 374-377.
- [43] T.L. Anderson, *Fracture Mechanics: fundamentals and applications* (1995) CRC Press.
- [44] A. Martín-Meizoso, J.M. Martínez-Esnaola, *Mecánica de la Fractura* (1999) TECNUN-University of Navarra.